RSC Advances

PAPER

View Article Online
View Journal | View Issue

Cite this: *RSC Adv.*, 2025, **15**, 44909

Sensitive superoxide dismutase detection *via* luminol–oxygen electrochemiluminescence enhanced by zero-dimensional carbon catalysts in mesoporous nanochannels

Huihua Zhang,[a] Lanlan Wu,[b] Fengna Xi *[b] and Baolin Zhang*[a]

Received 27th September 2025
Accepted 9th November 2025

DOI: 10.1039/d5ra07346d

rsc.li/rsc-advances

The detection of superoxide dismutase (SOD) is crucial for monitoring the antioxidant defense system. In this study, an electrochemical-assisted self-assembly (EASA) method was used to *in situ* grow amino-functionalized vertically ordered mesoporous silica film (NH_2-VMSF) on an ITO electrode, creating highly ordered nanochannel structures. Nitrogen-doped graphene quantum dots (NGQDs) were then confined within these channels *via* electrophoretic deposition, resulting in a composite electrode, NGQDs@NH_2-VMSF/ITO. The introduction of NGQDs significantly enhanced the electrode's catalytic activity for the oxygen reduction reaction (ORR), facilitating the generation of superoxide anion radicals ($O_2^{\bullet-}$) and promoting the electrochemical oxidation of luminol, which substantially increased the electrochemiluminescence (ECL) signal of the luminol–dissolved oxygen (DO) system. In the presence of SOD, $O_2^{\bullet-}$ is selectively eliminated by SOD, leading to a decrease in the ECL signal as the SOD concentration increases. This "signal-off" response enables highly sensitive detection of SOD. The developed ECL sensor demonstrated a linear relationship within the SOD concentration range of 0.005–5 μg mL^{-1}, with a limit of detection (LOD) as low as 0.87 ng mL^{-1} (S/N = 3). This work offers a reliable sensing platform for analyzing antioxidant activity and related disease biomarkers.

1. Introduction

Superoxide dismutase (SOD) is one of the most crucial antioxidant enzymes in the body.[1] Its active site is composed of metal ions (Cu^{2+}/Zn^{2+} or Mn^{2+}) coordinated with a protein scaffold, catalyzing the disproportionation of superoxide anions ($O_2^{\bullet-}$) to produce hydrogen peroxide and oxygen ($2O_2^{\bullet-} + 2H^+ \rightarrow H_2O_2 + O_2$).[2] The rate constant of this reaction is near the diffusion-controlled limit (2×10^9 M^{-1} s^{-1}), roughly 10^4 times faster than the spontaneous disproportionation of superoxide anions. SOD activity measurement is crucial for assessing the body's antioxidant capacity and oxidative stress levels, holding significant research and clinical value.[3] As the primary enzymatic defense against superoxide anions, SOD activity directly reflects the body's ability to combat oxidative damage. Alterations in SOD activity are closely associated with various diseases. For example, in the advanced stages of aging, diabetes, and neurodegenerative disorders, SOD activity is often markedly reduced, indicating a decline in antioxidant defense and enhanced oxidative damage. Conversely, during acute stress or in the early stages of certain diseases, SOD activity may increase compensatorily, suggesting an active response to free radical attacks. In practical applications, SOD activity detection not only serves as a key indicator for evaluating the efficacy of antioxidant drugs and health supplements but also aids in basic research to clarify physiological and pathological mechanisms, as well as the action mechanisms of environmental toxins.[4] Therefore, SOD activity detection is closely linked to oxidative stress, cellular health, and disease progression, providing essential evidence for disease diagnosis, health risk assessment, and therapeutic efficacy evaluation.

In recent years, various methods for the quantitative determination of SOD activity have been reported, including electron paramagnetic resonance (EPR),[5] enzyme-linked immunosorbent assay (ELISA),[6] high-performance liquid chromatography (HPLC),[7] and chemiluminescence (CL).[8] For example, EPR indirectly measures SOD activity by using spin trapping agents such as 5,5-dimethyl-1-pyrroline-*N*-oxide (DMPO) to capture free radicals. However, its application is limited due to the high cost of the instrumentation. ELISA, based on the immunological principle of antigen–antibody binding, can detect enzyme levels in liquid samples. However, it requires the preparation of specific antibodies for different types of SOD, which is a labour-intensive and time-consuming process. HPLC measures SOD activity by separating and quantifying the products of enzyme catalyzed reactions, offering high specificity and accuracy, but it

[a]*Third Hospital of Shanxi Medical University, Shanxi Bethune Hospital, Shanxi Academy of Medical Sciences, Tongji Shanxi Hospital, Taiyuan, 030032, China. E-mail: WBL88@126.com*

[b]*School of Chemistry and Chemical Engineering, Zhejiang Sci-Tech University, Hangzhou, 310018, China. E-mail: Fengnaxi@zstu.edu.cn*

requires complex sample preparation and has high equipment maintenance costs. CL is based on the catalytic oxidation of xanthine or hypoxanthine by xanthine oxidase under aerobic conditions, generating superoxide anion radicals, which react with luminol to produce a light signal. However, the sensitivity still requires further improvement. Developing convenient and rapid methods for SOD activity detection is of great significance.

Electrochemiluminescence (ECL) is an analytical technique that combines electrochemistry with chemiluminescence, offering advantages such as low background signals and ease of operation.[9–11] Due to these advantages, it has shown broad applications in fields such as biosensing, disease diagnosis, and environmental monitoring.[12–15] For instance, the contact-electrocatalysis effect of polytetrafluoroethylene (PTFE) particles were employed to drive the water oxidation reaction (WOR) and oxygen reduction reaction (ORR) under ultrasonication, generating superoxide anions ($O_2^{\bullet-}$) and hydroxyl radicals (HO$^\bullet$). These reactive oxygen species (ROS) then react with luminol, producing a strong ECL signal, thereby enabling sensitive detection of SOD.[16] However, this system relies on continuous ultrasonication to maintain electrocatalytic activity, which complicates operational standardization and limits signal stability. Liu *et al.* developed an ECL sensing system using CuInZnS quantum dots as the emitter and hydrogen peroxide (H_2O_2) as the co-reactant. Quantification of SOD was achieved by monitoring the competitive consumption of superoxide generated from H_2O_2 at the electrode interface. However, this method requires a relatively high negative scanning potential (approximately −2.5 V) to excite the strong ECL signal, resulting in a wide scanning potential range.[17] The anodic ECL of lucigenin (*N*,*N*-dimethyl-9,9′-biacridinium dinitrate) on a mesoporous Pt electrode can generate superoxide anions ($O_2^{\bullet-}$) through the oxidation of water or hydroxide ions. The addition of SOD quenches the ECL intensity, allowing for quantitative analysis of SOD.[18] However, the preparation of the mesoporous Pt electrode involves relatively complex procedures. Thus, convenient ECL detection of SOD is highly desirable.

Compared to expensive noble metal complexes (*e.g.*, tris(2,2′-bipyridyl)ruthenium(III)) with high ECL potential, luminol has gained considerable attention as an ECL emitter due to its lower oxidation potential and costless advantages.[19] To improve the ECL efficiency of luminol, H_2O_2 is often introduced as a co-reactant, wherein the ROS generated by its decomposition oxidize the luminol anion, enhancing the ECL signal.[20] However, H_2O_2 is prone to self-decomposition and high concentrations of H_2O_2 may exhibit toxicity to biological systems.[21] In contrast, dissolved oxygen (DO) in the electrolyte is a non-toxic and stable co-reactant, making it an ideal endogenous agent.[22] However, the (ORR process exhibits low kinetics, resulting in slow ROS generation and weak ECL signals in the luminol–DO system, which limits its application in high-sensitivity detection.[23] Therefore, the key strategy for enhancing the efficiency of the luminol–DO ECL system is the introduction of efficient catalysts to accelerate the ORR process, facilitating the generation of more ROS and thereby significantly boosting the ECL signal.

To date, various types of catalysts have been extensively explored. For example, single-atom catalysts (SACs), such as M–N–C structures (M = Fe, Co, Cu, *etc.*), exhibit high atom utilization and tunable electronic structures, enabling efficient catalysis of ORR.[24] They generate large amounts of $O_2^{\bullet-}$ and HO$^\bullet$, significantly enhancing the ECL signal. Double-atom catalysts (DACs) take advantage of the synergistic effect between two metal sites, further optimizing the O=O bond cleavage pathway and demonstrating superior catalytic activity compared to SACs.[25] In addition, some nanozymes (*e.g.*, cobalt oxide and cerium oxide nanoparticles) are used to catalyze the *in situ* generation of H_2O_2, thereby amplifying the ECL response.[26,27] Among various catalysts, carbon-based nanomaterials have shown unique properties and have exhibited several advantages.[28–30] Firstly, carbon materials (*e.g.*, graphene, carbon nanotubes) possess excellent conductivity, which promotes electron transfer at the electrode interface,[31–35] accelerates the ORR and oxidation of luminol, and improves the ECL reaction kinetics. Secondly, carbon nanomaterials have high specific surface areas, providing abundant active sites for catalytic reactions.[36–39] Thirdly, compared to noble metals or metal oxides, carbon materials generally exhibit superior stability in electrochemical environments, are less prone to aggregation, dissolution, or deactivation, and have low cytotoxicity, which is particularly important for biosensing applications.[40] Fourthly, carbon materials are cost-effective, with potential for large-scale applications. Therefore, developing carbon-based catalysts with tunable performance, structural stability, and good biocompatibility provides a promising path for constructing high-sensitivity, high-stability ECL analytical platforms. Amongst, graphene quantum dots (GQDs), as zero-dimensional nanocarbon materials, exhibit low cytotoxicity, high stability, and excellent biocompatibility, showing extensive application potential in ion detection, biological imaging, and optical sensing.[41,42] Heteroatom doping has been proven to be an effective strategy to enhance the catalytic performance of GQDs.[43] By introducing heteroatoms, electronic structure, surface properties, and chemical activity of NGQDs can be modulated, thus enhancing their intrinsic catalytic ability. Compared to undoped GQDs, doped materials typically have more active sites and show greater potential.[44] However, the high water dispersibility of GQDs also causes them to easily detach after modification onto electrodes, resulting in reduced electrode stability and reproducibility. Therefore, improving the stability and catalytic performance of GQDs-modified electrodes has become a critical issue to address.

Vertically-ordered mesoporous silica film (VMSF) consists of highly ordered nanochannel arrays oriented perpendicularly to the substrate.[45,46] This unique architecture provides significant advantages, enabling promising applications in electrochemical sensing, separation, and confined-space catalysis.[47–49] The uniform nanochannels serve as ideal confined domains for the stable immobilization of nanocatalysts.[50–52] The silica framework imparts excellent mechanical strength, allowing VMSF to maintain structural integrity and functional stability under complex electrochemical or biological conditions.[53] Abundant surface silanol groups facilitate *in situ* growth or post-modification with functional moieties such as amino, thiol, or carboxyl groups, leading to flexible regulation of surface

chemistry.[54,55] Moreover, VMSF exhibits good antifouling properties and biocompatibility.[56,57] Specifically, its ordered nanochannels impose a size-exclusion effect that efficiently blocks biomacromolecules (*e.g.*, proteins), preventing electrode fouling while preserving compatibility in biological matrix.[58–60] These features significantly enhance the reliability and lifetime of direct detection in complex samples such as serum or whole blood.[61] Owing to these merits, VMSF represents an ideal functional platform for the confinement of ultrasmall carbon nanomaterials to construct high-performance biosensing interfaces.

In this work, ultrasmall nanochannels were employed as a confined space to fabricate a highly stable nitrogen-doped graphene quantum dots (NGQDs)-modified electrode. The NGQDs on the electrode effectively catalyze oxygen to generate a high concentration of $O_2^{\bullet-}$, thereby enhancing the ECL signal in the luminol–DO system. The employed VMSF was surface-modified with amino groups (NH_2-VMSF). NGQDs were synthesized *via* a one-step, bottom-up hydrothermal method and confined inside the nanocapillaries using electrophoresis. In the presence of SOD, the $O_2^{\bullet-}$ reacts with SOD, leading to the decrease of the luminol ECL signal. Based on this mechanism, a signal-off ECL sensing platform was successfully constructed, enabling high-sensitivity detection of SOD.

2. Experimental

2.1 Materials and reagents

$NaH_2PO_4 \cdot 2H_2O$, $Na_2HPO_4 \cdot 12H_2O$, $NaHCO_3$, NaOH, $NaNO_3$, HCl, $K_3[Fe(CN)_6]$, $Ru(NH_3)_6Cl_3$, $NH_3\ H_2O$ (≥25 wt%), C_2H_5OH (99.8% purity), acetone (C_3H_6O), potassium hydrogen phthalate (KHP), cetyltrimethylammonium bromide (CTAB), tetraethyl *ortho*-silicate (TEOS), fetal bovine serum, 3-aminopropyltriethoxysilane (APTES), 1-aminopyrene (1-AP), benzoquinone (BQ), *tert*-butyl alcohol (TBA), and luminol were purchased from Aladdin Biochemical Technology Co., Ltd (Shanghai, China). SOD was obtained from Sangon Biotech Co., Ltd. All reagents were used without further purification. ITO conductive glass (sheet resistance <17 Ω sq^{-1}, ITO thickness: 100 ± 20 nm) was sourced from Kaivo Electronic Components Co., Ltd (Zhuhai, China). Before use, the ITO electrodes were cleaned as follows: first, the electrodes were soaked overnight in a 1 M NaOH solution to remove organic impurities and some inorganic contaminants from the surface. Next, they were sequentially sonicated in acetone, ethanol, and deionized water for 10 minutes each. Finally, the electrodes were dried with nitrogen gas or at 60 °C. The cleaned electrodes were stored at room temperature for future use, with an effective electrode area of 0.5 cm × 1 cm used in the experiments.

2.2 Characterizations and instrumentations

The morphology of NH_2-VMSF was examined using transmission electron microscopy (TEM, Hitachi HT7700, Japan) and scanning electron microscopy (SEM, Hitachi SU8010, Japan). Fluorescence imaging of the surfaces of various modified electrodes was carried out with a laser confocal scanning microscope (CLSM, Olympus FV1000, Japan), employing an excitation wavelength of 488 nm. Electrochemical performance was performed on an Autolab electrochemical workstation (Metrohm, Switzerland, PGSTAT302N), with a scan rate set at 50 mV s^{-1}. ECL measurements were performed using the MPI-E II system (Xi'an RuiMai Analytical Instruments Co., Ltd, China), at a scan rate of 100 mV s^{-1}. Unless otherwise specified, the PMT bias voltage was set at 700 V for ECL measurements. The elemental composition and chemical states of the material surfaces were investigated *via* X-ray photoelectron spectroscopy (XPS, PHI 5300, PerkinElmer, USA), utilizing an Mg Kα X-ray source (power: 250 W, voltage: 14 kV). The optical characteristics of NGQDs were analyzed through UV-Vis absorption spectroscopy (Shimadzu UV-2450, Japan) and fluorescence spectroscopy (HORIBA FluoroMax-4, USA). All electrochemical and ECL measurements were conducted in a three-electrode setup: bare or modified ITO electrodes as the working electrode, a platinum wire as the counter electrode, and an Ag/AgCl (saturated KCl) electrode as the reference.

2.3 Preparation of nanochannel array modified electrode with confined NGQDs

NGQDs were synthesized using a one-step hydrothermal method, with 1-aminopyrene as the carbon source and ammonia solution as the nitrogen source under alkaline conditions.[43] Using electrochemical-assisted self-assembly (EASA), amino-functionalized vertically ordered mesoporous silica films (NH_2-VMSF/ITO) were fabricated on ITO substrates using TEOS and APTES as primary precursors.[62] The electrode was then immersed in a 0.3 mg mL^{-1} NGQDs solution and NGQDs were electrophoretically deposited at a constant potential of +0.8 V for 15 minutes, which confined the NGQDs within NH_2-VMSF. The resulting electrode was labelled as NGQDs@NH_2-VMSF/ITO.

2.4 ECL detection of SOD and analysis of real samples

The prepared NGQDs@NH_2-VMSF/ITO electrode was immersed in PBS solution (0.01 M, pH = 7.4) containing varying concentrations of SOD and 100 μM luminol. Electrochemical measurements were performed using cyclic voltammetry (CV) in the potential range of −1.0 to 0.8 V with a scan rate of 100 mV s^{-1}, while monitoring the changes in the ECL signal. For the analysis of real samples, a standard addition method was employed, with fetal bovine serum (FBS) selected as the complex matrix for method validation. Prior to analysis, FBS samples were diluted 100-fold with PBS (0.01 M, pH = 7.4). Known concentrations of SOD were added to the pretreated samples to evaluate the applicability and accuracy of the detection method in real biological samples.

3. Results and discussion

3.1 Construction of the ECL sensor

As shown in Fig. 1, a highly sensitive ECL sensor for SOD detection was developed based on NGQDs and functionalized mesoporous nanochannel array film. The sensor was built on ITO conductive

glass, chosen for its excellent electrical conductivity and optical transparency, which are ideal properties for constructing ECL devices. EASA was employed to *in situ* grow a highly ordered, vertically oriented NH_2-VMSF on the ITO surface. TEOS and amino-contained APTES were used as mixed precursors under mild electrochemical conditions.[35] The resulting film exhibited a uniform nanoporous array structure, and the surface amino groups provided reactive sites for subsequent quantum dot immobilization. The resulting electrode was labelled NH_2-VMSF/ITO. Then, the pre-synthesized NGQDs were efficiently confined inside the nanochannels using a constant potential electrophoretic deposition method. The electrode was applied +0.8 V for 15 minutes, during which the NGQDs were electrostatically fixed within the nanochannels due to the interaction between the surface charges of the NGQDs and the amino groups within the nanochannels. This composite electrode was designated as NGQDs@NH_2-VMSF/ITO (Fig. 1A). This strategy not only enhanced the loading capacity and uniform dispersion of the NGQDs but also significantly improved the ECL efficiency of the luminol–DO system (Fig. 1B). The underlying mechanism is that the NGQDs act as catalytic centers, promoting the generation of $O_2^{\bullet-}$ from dissolved oxygen, thereby greatly enhancing the ECL signal. During the detection process, the addition of SOD reduced $O_2^{\bullet-}$ concentration and consequently decreased the ECL reaction between luminol and $O_2^{\bullet-}$. This results in a significant decrease in the signal, which exhibits a linear relationship with the SOD concentration, enabling rapid and highly sensitive quantification of SOD.

3.2 Characterization of NGQDs

To comprehensively evaluate the characteristics of the synthesized nitrogen-doped graphene quantum dots (NGQDs), UV–Vis absorption and fluorescence (FL) spectra were recorded (Fig. 2A and B). The UV–Vis spectrum exhibited a pronounced absorption band at ~350 nm, which can be ascribed to n–π* transitions of C–O and C–N bonds, confirming that nitrogen incorporation changes the electronic structure of the carbon framework. Upon excitation at 365 nm, NGQDs displayed a strong emission centered at ~500 nm with bright green luminescence. This emission behaviour is associated with surface states introduced by nitrogen dopants, which facilitate radiative recombination, highlighting the favourable photoluminescent properties of NGQDs.[63]

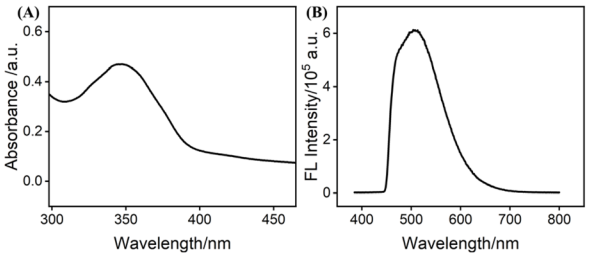

Fig. 2 (A and B) UV–Vis (A) and fluorescence (B) spectra of NGQDs.

The chemical composition and bonding environment of NGQDs were further investigated by X-ray photoelectron spectroscopy (XPS), as shown in Fig. 3A–D. The survey spectrum (Fig. 3A) confirmed the presence of C, O, and N elements, indicating successful nitrogen incorporation into the carbon lattice. The high-resolution C 1s spectrum (Fig. 3B) revealed peaks at 284.5 eV, 286.2 eV, and 288.6 eV, corresponding to sp^2-hybridized C=C, C–N, and C=O bonds,[64] respectively, suggesting the co-existence of aromatic domains, nitrogen dopants, and oxygen-containing groups. The N 1s spectrum (Fig. 3C) exhibited a major signal at ~399.5 eV, which upon deconvolution could be resolved into three distinct nitrogen species including pyridinic N (398.4 eV, sp^2-hybridized), pyrrolic N (399.5 eV, sp^3-hybridized), and graphitic N (401.0 eV, substitutional N).[65] These nitrogen functionalities are expected to tune the electronic structure and catalytic performance of NGQDs. In addition, the O 1s spectrum (Fig. 3D) displayed characteristic peaks at 531.4 eV and 532.0 eV, attributable to C–O and C=O bonds,[64] indicating abundant hydroxyl and carboxyl groups on the NGQDs. Such hydrophilic moieties contribute to their excellent aqueous dispersibility.

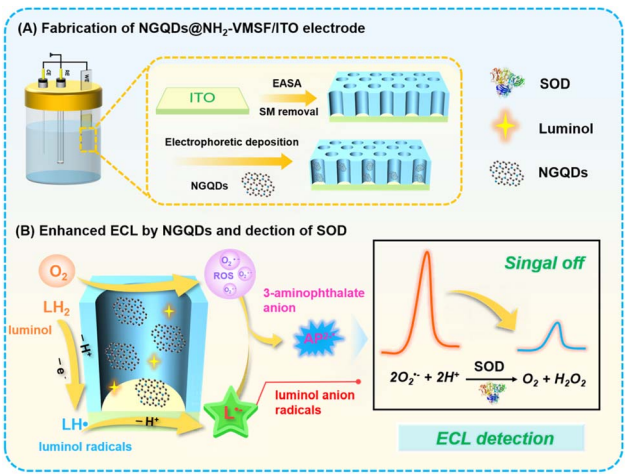

Fig. 1 Illustration for (A) fabrication of NGQDs@NH_2-VMSF/ITO electrode and (B) enhanced ECL by NGQDs and detection of SOD.

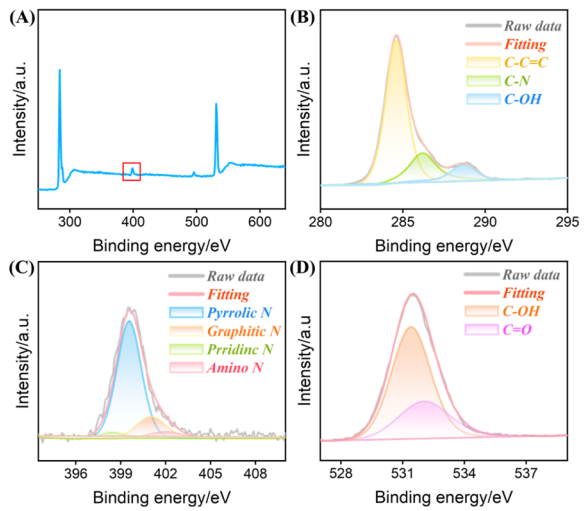

Fig. 3 (A) XPS survey spectrum of NGQDs. (B–D) High-resolution XPS spectra of NGQDs: (B) C 1s, (C) N 1s, and (D) O 1s.

3.3 Characterization of NH_2-VMSF/ITO and NGQDs@NH_2-VMSF/ITO electrode

The morphology and structural features of the nanochannel array electrodes were systematically examined using transmission electron microscopy (TEM) and scanning electron microscopy (SEM). TEM images (Fig. 4A and B) revealed that the NH_2-VMSF film possesses highly ordered, vertically oriented nanochannels arranged in a hexagonal close-packed configuration, with uniform pore size and well-aligned channels, demonstrating excellent long-range order. Cross-sectional TEM analysis indicated a film thickness of approximately 75 nm, confirming that the EASA method successfully generated a mesoporous silica layer of controllable thickness on the ITO substrate. SEM surface images (Fig. 4C) showed a smooth, continuous film without visible cracks or defects, indicating high-quality formation. Cross-sectional SEM (Fig. 4D) clearly resolved the three-layer architecture: the glass substrate at the bottom, the ITO conductive layer (~100 nm), and the NH_2-VMSF functional film (~75 nm), consistent with TEM measurements. These observations confirm that NH_2-VMSF uniformly and completely covers the ITO electrode surface, providing a reliable structural foundation for subsequent ECL sensing. Laser confocal scanning microscopy (CLSM) was used to visualize NGQDs confined within the nanochannels. Under 488 nm excitation, no fluorescence was observed for NH_2-VMSF/ITO without NGQDs (Fig. 4E), whereas NGQDs@NH_2-VMSF/ITO exhibited uniform and intense green fluorescence (Fig. 4F), directly confirming that NGQDs were successfully confined within the nanochannels while retaining strong luminescence.

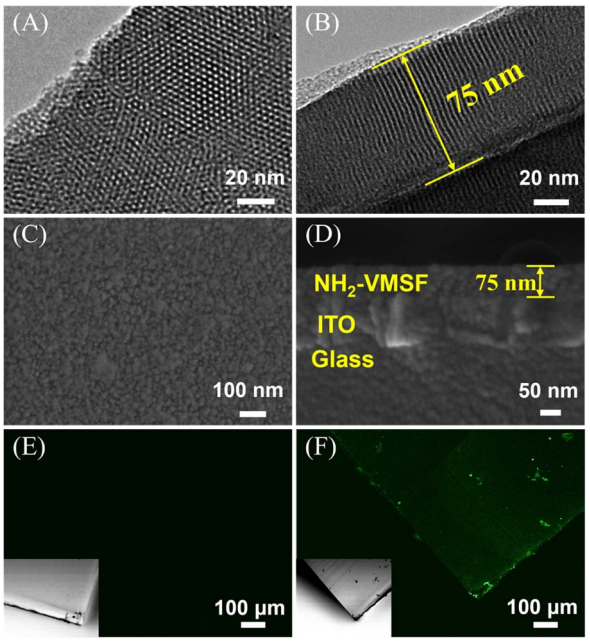

Fig. 4 (A and B) TEM images of the surface (A) and cross-section (B) of NH_2-VMSF. (C and D) SEM images of the surface (C) and cross-section (D) of the NH_2-VMSF/ITO electrode. (E and F) Confocal laser microscopy images of NH_2-VMSF/ITO (E) and NGQDs@NH_2-VMSF/ITO (F). The insets show the corresponding bright-field images. Excitation wavelength: 488 nm.

To further assess the charge-selective permeability of NH_2-VMSF, CV was used to compare the electrochemical behaviour of redox probes with different charges (Fig. 5A and B). For the negatively charged $[Fe(CN)_6]^{3-/4-}$ probe, bare ITO exhibited well-defined reversible redox peaks. In contrast, SM@NH_2-VMSF/ITO electrode, in which the pore openings were blocked by surfactant micelles, showed negligible current, indicating effective pore blockage and hindered mass transport. Notably, NH_2-VMSF/ITO electrodes displayed significantly enhanced redox currents for the anionic probe, which can be attributed to the protonation of amino groups (–NH_2) within the mesopores under near-neutral conditions to form positively charged –NH_3^+ groups.[66] Electrostatic attraction between these groups and the negatively charged probe facilitates probe transport and accumulation. Conversely, for the positively charged $Ru(NH_3)_6^{3+}$ probe, the redox current at NH_2-VMSF/ITO was lower than that at bare ITO, reflecting electrostatic repulsion from the positively charged pore walls. This opposite behaviour toward cationic and anionic probes demonstrates that NH_2-VMSF not only maintains structural integrity but also exhibits excellent charge-selective permeability, providing a foundation for interference-resistant detection in complex matrices. The confinement of NGQDs within the nanochannels was further evidenced. Compared to the NH_2-VMSF/ITO electrode, the NGQDs @NH_2-VMSF/ITO electrode exhibited a decreased peak current for $[Fe(CN)_6]^{3-/4-}$ and increased peak current for $Ru(NH_3)_6^{3+}$, which was attributed to the introduction of negatively charged NGQDs.

3.4 Stability of NGQDs within nanochannels

The practical application of ECL sensors depends on the stability of the luminescence signal. To systematically evaluate the stability of NGQDs on different electrode substrates, the ECL performance and signal variation of NGQDs-modified electrodes were compared in luminol–DO system. Both ITO electrodes and NH_2-VMSF modified were investigated under continuous cyclic scanning (Fig. 6A and B). As shown, compared with unmodified bare electrodes, electrodes prepared by the drop-coating method (NGQDs(drop-coating)/ITO and NGQDs(drop-coating)@NH_2-VMSF/ITO) exhibited a significant enhancement in ECL intensity, confirming the catalytic

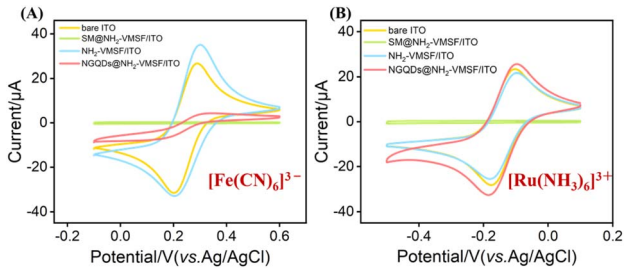

Fig. 5 CV curves of bare ITO, SM@NH_2-VMSF/ITO, NH_2-VMSF/ITO and NQGDs@NH_2-VMSF/ITO in (A) $[Fe(CN)_6]^{3-}$ or (B) $[Ru(NH_3)_6]^{3+}$ solutions. The redox concentration was 0.5 mM and the electrolyte was 0.05 M KHP solution. Scan rate in CV measurement was 50 mV s^{-1}.

sensitization effect of NGQDs toward the luminol–DO system. However, both drop-cast electrodes showed pronounced signal decay over ten consecutive scans. Specifically, the ECL intensity of NGQDs(drop-coating)/ITO decreased sharply from 9059 a.u. to 4198 a.u. (RSD = 27%, Fig. 6C), indicating poor stability, while NGQDs(drop-coating)@NH_2-VMSF/ITO declined from 5102 a.u. to 3592 a.u. (RSD = 12%, Fig. 6D). These results suggest that although drop-coating is simple, it cannot achieve long-term stable immobilization of NGQDs. The instability is likely due to the high water solubility of NGQDs, which facilitates detachment. At the same time, drop-coating tends to form thick, loose layers that leads to remarkable signal loss.

In contrast, electrodes fabricated *via* electrophoretic deposition demonstrated both higher initial ECL intensity and significantly improved stability. The NGQDs (electrophoresis)/ITO electrode prepared by electrophoresis showed a slow decrease from 11 711 a.u. to 9481 a.u. (RSD = 7%, Fig. 6E), reflecting a much lower decay rate than the drop-cast samples, likely due to the uniform distribution of NGQDs achieved under the applied electric field. Remarkably, when NGQDs were confined within the nanochannels of NH_2-VMSF by electrophoretic deposition, the NGQDs@NH_2-VMSF/ITO electrode exhibited only a minor decrease in ECL intensity from 9618 a.u. to 9196 a.u. (RSD = 1.6%, Fig. 6F), demonstrating high signal stability.

These observations indicate that while drop-coating can initially enhance ECL response, the physical adsorption of NGQDs onto the electrode surface leads to easy detachment and aggregation during repeated electrochemical cycling, resulting in ECL signal decay. By contrast, electrophoretic deposition drives NGQDs to migrate directionally and adhere more firmly to the electrode. The vertically ordered mesoporous structure of NH_2-VMSF provides a spatial confinement effect, while surface amino groups interact with NGQDs *via* electrostatic and dipolar interactions, enabling stable immobilization within the nanochannels. Consequently, NGQDs@NH_2-VMSF/ITO electrode exhibit both high and stable ECL signals.

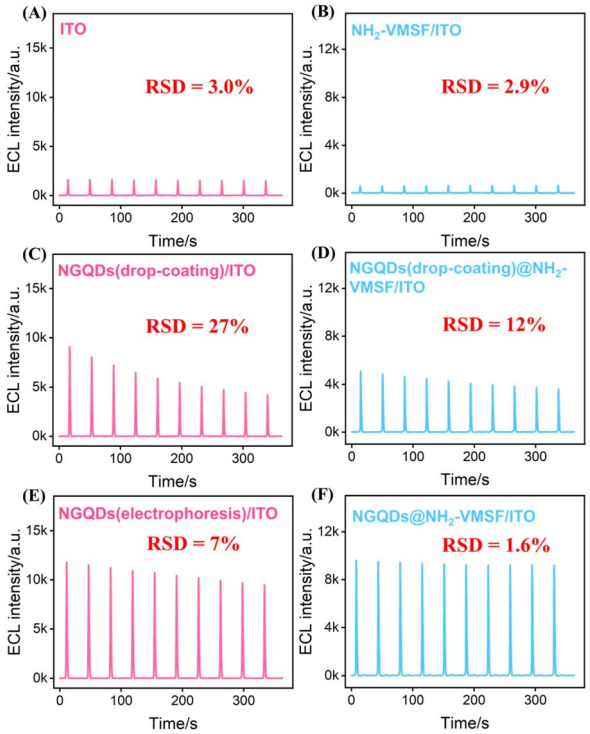

Fig. 6 ECL intensity–time curves obtained at (A) ITO, (B) NH_2-VMSF/ITO, (C) NGQDs(drop-coating)@ITO, (D) NGQDs(drop-coating)@NH_2-VMSF/ITO, (E) NGQDs(electrophoresis)@ITO, and (F) NGQDs@NH_2-VMSF/ITO electrodes. The PMT voltage was set at 600 V.

3.5 Mechanism of NGQDs-enhanced ECL and SOD-quenched ECL in the luminol–DO system

The emission efficiency of luminol–DO system is closely related to ROS generation and the oxidation of luminol. In this work, NGQDs were confined within the nanochannels of NH_2-VMSF to construct NGQDs@NH_2-VMSF/ITO electrodes, and the enhancement mechanism of ECL was investigated. As shown in Fig. 7A, confinement of NGQDs within the NH_2-VMSF led to nearly a five-fold increase in ECL intensity compared to NH_2-VMSF/ITO without NGQDs, demonstrating a pronounced signal amplification effect. CV measurements were further performed in air-saturated PBS and in PBS containing 100 μM luminol. In air-saturated PBS, the NGQDs@NH_2-VMSF/ITO electrode exhibited a positive shift in the oxygen reduction peak and an increase in the cathodic current from −33.8 μA to −50.2 μA relative to NH_2-VMSF/ITO (Fig. 7B), indicating that NGQDs effectively accelerate the ORR, enhance electron transfer, and reduce overpotential. This catalytic behaviour might be attributed to the defect sites and active centers introduced by nitrogen doping, along with the intrinsic electrocatalytic properties of NGQDs. Under N_2 atmosphere, the reduction peak nearly disappeared, confirming that the observed current originates from dissolved oxygen. These results indicated that NGQDs efficiently catalyze O_2 reduction and promote the formation of ROS. Upon addition of luminol (Fig. 7C), the anodic oxidation peak near +0.8 V increased from 2.8 μA to 7.90 μA at NGQDs@NH_2-VMSF/ITO, demonstrating that NGQDs not only facilitate oxygen reduction but also significantly enhance the electrochemical oxidation of luminol. This effect likely arises from improved electron transfer at the electrode surface and the catalytic promotion of luminol deprotonation to generate luminol radical anions, providing abundant precursors for the subsequent ECL reaction. Thus, NGQDs play a dual role in the luminol–DO including catalyzing O_2 reduction to generate ROS and promoting luminol oxidation, which together synergistically amplify the ECL signal.

As shown in Fig. 7D, during the forward scan (0 → 0.8 → −1.0 → 0 V), the first cycle yielded a negligible ECL signal with only a weak peak of 466 a.u. A strong ECL peak (15 050 a.u.) then emerged in the second cycle.[67] In contrast, during the reverse scan (0 → −1.0 → 0.8 → 0 V, Fig. 7E), a strong ECL peak (13 974 a.u.) was observed immediately in the first cycle, as the potential initially entered the cathodic region and triggered the oxygen reduction reaction (ORR). The direct comparison of the first-cycle peaks (13 974 a.u. *vs.* 466 a.u.) showed that the ECL

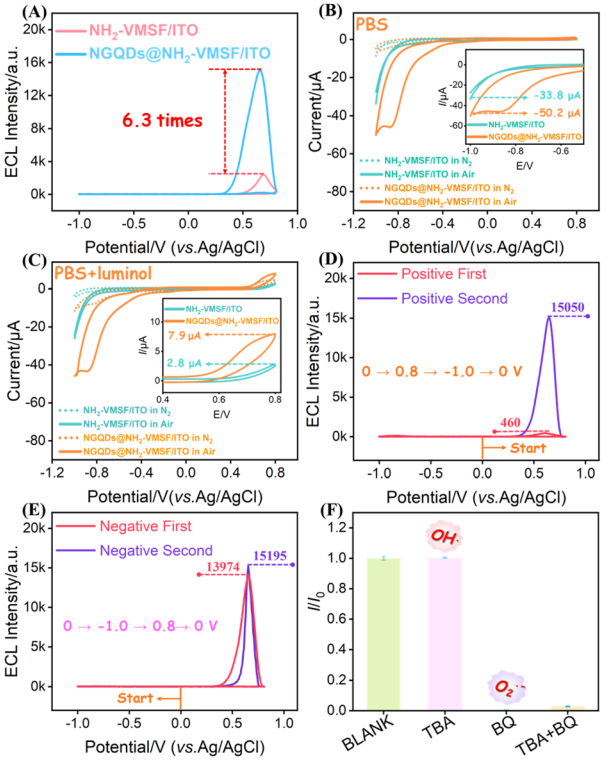

Fig. 7 (A) ECL–potential curves of NH_2-VMSF/ITO and NGQDs@NH_2-VMSF/ITO electrodes. CV curves of NH_2-VMSF/ITO and NGQDs@NH_2-VMSF/ITO electrodes in (B) PBS (0.01 M, pH 7.4) and (C) 100 μM luminol solution. ECL–potential curves of NGQDs@NH_2-VMSF/ITO electrode under (D) forward and (E) reverse scans (starting potential = 0 V). (F) Changes in ECL intensity after the addition of different radical scavengers, where I and I_0 denote the ECL signals in the presence and absence of radical scavengers, respectively. The concentrations of BQ and TBA were 100 μM and 1 mg mL^{-1}, respectively. The electrolyte solution was PBS (0.01 M, pH 7.4) containing 100 μM luminol.

signal from the reverse scan was 30 times stronger than that from the forward scan. This distinct difference demonstrates that the ORR and the accumulation of ROS were prerequisites for the intense ECL signal.[68] Without a prior ORR process, the system emitted almost no light and a strong signal appeared only upon reverse scanning after sufficient ROS has been generated. These results confirm an "ORR-first to light" mechanism.

To identify the dominant ROS involved, radical scavenger experiments were conducted (Fig. 7F). Addition of the hydroxyl radical scavenger *tert*-butyl alcohol (TBA) caused negligible change in ECL intensity, indicating that HO$^{\bullet}$ is not the key active species. In contrast, addition of the superoxide scavenger *p*-benzoquinone (BQ) nearly completely suppressed the ECL signal, and simultaneous addition of TBA and BQ fully abolished the emission. These results confirm that $O_2^{\bullet-}$ is the primary reactive intermediate responsible for ECL in the luminol–dissolved oxygen system, playing a central role in promoting luminol oxidation and light emission.[69,70]

As shown in Fig. S1A (in SI), the luminol–DO system produced a strong ECL signal of 15 128 a.u., which decreased significantly to 6069 a.u. after SOD addition. Thus, SOD quenched the ECL of luminol–DO, that was ascribed that SOD catalyzed the dismutation of $O_2^{\bullet-}$ into H_2O_2, reducing $O_2^{\bullet-}$ concentration and leading to decreased ECL. As H_2O_2 was also a co-reactant of luminol, control experiment was further performed to verify that SOD-generated H_2O_2 fails to sustain ECL. As shown in Fig. S1B (SI), in the luminol–H_2O_2 (N_2-purged) system, externally added H_2O_2 acted as a co-reactant to generate an ECL signal of 9553 a.u.; however, upon SOD introduction, the signal dropped sharply to 821 a.u. Thus, in the luminol ECL system using H_2O_2 as a co-reactant, the presence of SOD prevented H_2O_2 from maintaining or enhancing the ECL signal. Furthermore, a remarkable reduction in ECL was observed after adding BQ in luminol–H_2O_2 (N_2-purged) system, confirming the $O_2^{\bullet-}$-supported route in ECL generation of luminol–H_2O_2 system (Fig. S2, SI). These results demonstrate that SOD-generated H_2O_2 fails to sustain ECL. SOD may reduce the net photon output, leading to a signal-off mode.

As illustrated in Fig. S3 (SI), the mechanism for the NGQDs-enhanced ECL of the luminol–DO system and the subsequent detection of SOD can be divided into three consecutive steps. First, the generation of ROS. Specifically, dissolved oxygen was electrocatalytically reduced at the electrode surface by NGQDs to produce $O_2^{\bullet-}$, which served as the crucial ROS for the subsequent ECL reaction. Subsequently, the ECL reaction occurred. Luminol (LH_2) was deprotonated to form the luminol anion (LH^-), which was then oxidized at the electrode to generate the corresponding luminol radical intermediate ($L^{\bullet-}$). This radical reacted with $O_2^{\bullet-}$ to form the excited-state aminophthalate dianion (AP^{2-}*), which emitted photons ($h\nu$) upon relaxation to its ground state, producing the ECL signal. In the presence of SOD, the enzyme catalyzed the dismutation of $O_2^{\bullet-}$ into oxygen and H_2O_2, thereby reducing the concentration of $O_2^{\bullet-}$ and leading to a corresponding decrease in the ECL intensity.

3.6 Optimization of the fabrication of NGQDs@NH_2-VMSF/ITO electrode

To enhance the performance of the ECL sensor, the electrophoretic deposition conditions of NGQDs on NH_2-VMSF/ITO electrodes were optimized, focusing on two critical parameters including deposition potential and deposition time. The results indicate that ECL intensity exhibits a characteristic rise-and-fall trend with increasing deposition potential or prolonging deposition time (Fig. 8). Under relatively low potentials or short deposition durations, increasing the deposition voltage or extending the time enhances the electrophoretic driving force, facilitating more efficient migration of NGQDs into the nanopores of NH_2-VMSF. This leads to a higher loading of quantum dots within the nanochannels, thereby significantly amplifying the ECL response. However, excessively high potential or overly long deposition can overload the nanochannels, potentially causing pore blockage. Such overloading not only hinders mass transport and electron transfer but may also saturate active sites on the electrode surface and induce luminescence quenching, resulting in a marked decrease in ECL intensity. Thus, the optimal preparation

conditions were determined to be deposition at +0.8 V for 15 minutes to achieve maximum ECL performance.

3.7 ECL detection of SOD

Under the optimized conditions, the NGQDs@NH_2-VMSF/ITO electrode was employed for ECL detection of SOD (Fig. 9A). The sensing mechanism relies on the specific catalytic dismutation of $O_2^{\bullet-}$ by SOD, which consumes superoxide radicals in the system, thereby suppressing the ECL reaction between luminol and $O_2^{\bullet-}$. As a result, the ECL intensity decreased progressively with increasing SOD concentration. Experimental results demonstrated a well-defined linear relationship between ECL intensity and the logarithm of SOD concentration (log C_{SOD}) over the 5 ng mL^{-1} to 5 μg mL^{-1} range (Fig. 9B). The linear regression equation was IECL = −2406 log C + 14 746 with a correlation coefficient of R^2 = 0.998. The limit of detection (LOD) was determined based on a signal-to-noise ratio (S/N) of 3. The noise level was characterized by the standard deviation (SD) of the blank signal, which was measured from three independent replicates (15 110 a.u., 15 030 a.u., 15 009 a.u.) in the absence of the target analyte. The average blank signal (X_{b1}) was 15 049 and the SD was 53.29. The slope (k) and intercept (b) of the regression equation were −2406 and 14 746, respectively. Based on S/N = 3, the noise level (X_L) was calculated using the formula $X_L = X_{b1} - k \times S_{b1} = 15\,049 - 3 \times 53.29 = 14\,889$. The LOD was then determined as LOD = $10^{[(X_L - b)/a]} = 10^{[(14\,889 - 14\,746/-2406)]}$ = 0.87 ng mL^{-1}. Comparison of the detection performance of SOD by different analytical methods was shown in Table S1.[8,18,71–74] The LOD obtained with the developed method was lower than ECL detection based on mesoporous platinum modified gold electrode (mesoporous Pt/AuE),[18] or multi-wall carbon nanotube/Au nanoparticles modified glassy carbon electrode (MWNT/nano-Au/GCE),[71] or polyamidoamine/titanate nanotubes modified GCE (PAAD/TiNTs/GCE),[72] or 3-decyl-1-(ferrocenylmethyl)-imidazolium bis (trifluoromethylsulfonyl) amide salts-hydroxy-functionalized graphene/Nafion modified GCE ([DFIM][Tf_2N]-HGN/Nafion/GCE).[73] The LOD obtained with the present method was also lower than the chemiluminescence (CL) sensing method using 1,4-dithiothreitol/*N*,*N*-dimethyl-9,9′-biacridinium dinitrate (DTT/Lucigenin)[8] or *N*-hydroxyphthalimide/lucigenin (NHPI-lucigenin).[74] In addition, the ECL sensor developed in this work operated at pH 7.4, which was close to the physiological pH of biological samples, offering advantage and convenience over

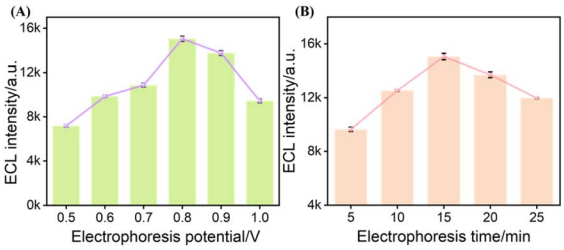

Fig. 8 ECL responses of NGQDs@NH_2-VMSF/ITO electrodes prepared at different electrophoretic potentials (A) and electrophoresis times (B).

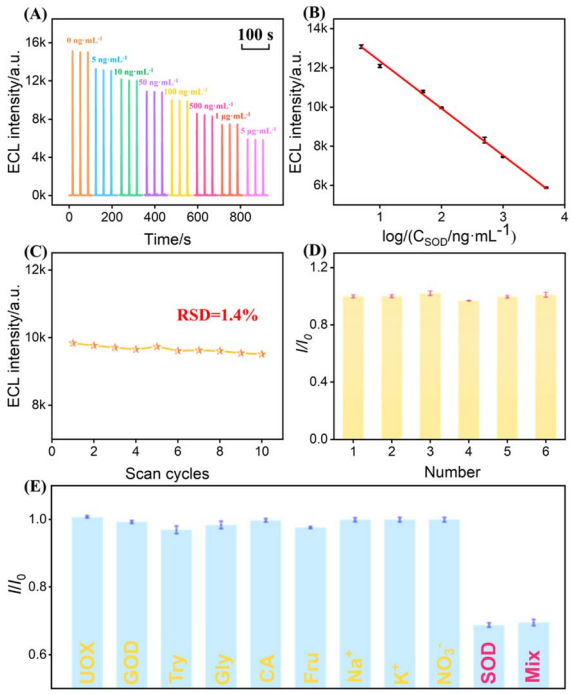

Fig. 9 (A) ECL intensity–time curves of NGQDs@NH_2-VMSF/ITO electrodes after interaction with different concentrations of SOD (0.005–5 μg mL^{-1}). (B) Linear regression curve of ECL intensity *versus* the logarithm of SOD concentration. Stability (C) and reproducibility (D) of the NGQDs@NH_2-VMSF/ITO electrode. (E) Relative change in ECL intensity of NGQDs@NH_2-VMSF/ITO electrodes before (I_0) and after (I) the addition of different substances. The concentrations of Na^+, K^+, and NO_3^- were 1 mM, while those of UOX, GOD, Try, Gly, CA, and Fru were 10 μg mL^{-1}.

detection that require highly alkaline conditions (*e.g.* pH 11). The constructed sensor employed ultrasmall nanochannels for the stable confinement of NGQD nanocatalysts, thereby enhancing the ECL of the luminol–DO system and enabling the sensitive detection of SOD *via* signal quenching. The fabricated sensor exhibits advantages including high sensitivity, low limit of detection, and operational simplicity.

The stability, reproducibility, selectivity, and anti-interference performance of the sensor were evaluated. Continuous ECL scanning over ten cycles in PBS containing 100 μM luminol and 100 ng mL^{-1} SOD yielded a relative standard deviation (RSD) of only 1.4% (Fig. 9C), confirming good signal stability. Reproducibility was assessed using six independently prepared electrodes (Fig. 9D), all of which exhibited consistent ECL responses with negligible variation, demonstrating the reliability of the fabrication method.

Selectivity tests were performed using common potential interferents, including uricase (UOX), glucose oxidase (GOD), trypsin (Try), glycine (Gly), and citrate (CA) (Fig. 9E). Only SOD and SOD-containing mixtures induced significant signal suppression, whereas other substances caused negligible changes, highlighting the high specificity of the sensor toward SOD.

The applicability of the ECL sensor for real sample analysis was further evaluated using a standard addition method in 100-fold diluted fetal bovine serum (FBS). The recoveries ranged

Table 1 Determination of SOD in FBS using the standard addition method

Sample	Added ($\mu g\ mL^{-1}$)	Found[a] ($\mu g\ mL^{-1}$)	RSD (%)	Recovery (%, $n = 3$)
FBS[a]	0.05	0.051	1.5	102
	0.50	0.52	2.4	104
	5.00	5.4	0.6	108

[a] The serum samples were diluted 100 times with PBS (0.01 M, pH = 7.4).

from 102% to 108%, with RSD values below 3.0% for three parallel measurements (Table 1), confirming the reliability in complex biological matrices.

4. Conclusions

Based on the specific scavenging activity of SOD toward $O_2^{\bullet-}$, a signal-off ECL sensor with high sensitivity was successfully developed for rapid detection of SOD. The sensor employs an ITO electrode modified with amino-functionalized vertically ordered mesoporous silica films, NH_2-VMSF, as the supporting electrode, onto which NGQDs were efficiently and uniformly confined within the nanochannels *via* electrophoretic deposition. The incorporation of NGQDs significantly enhanced the catalytic activity of the electrode toward oxygen reduction, promoting $O_2^{\bullet-}$ generation and facilitating the electrochemical oxidation of luminol, thereby greatly amplifying the ECL emission of the luminol–dissolved oxygen system. In this sensing mechanism, SOD, as the target analyte, catalyzed the dismutation of $O_2^{\bullet-}$, reducing the concentration of reactive radicals in the system and resulting in a concentration-dependent decrease in ECL intensity. This response enabled the establishment of a quantitative relationship between SOD concentration and ECL signal decrease, allowing sensitive detection of SOD. The sensor exhibited a linear response over a wide concentration range of 5 ng mL^{-1} to 5 $\mu g\ mL^{-1}$, with a detection limit as low as 0.87 ng mL^{-1}, demonstrating good analytical performance. The developed platform combines operational simplicity, rapid response, high reproducibility, and selectivity, making it suitable for convenient quantification of SOD. Furthermore, it holds promise for early diagnosis and mechanistic studies of oxidative stress-related diseases, including inflammation and neurodegenerative disorders. This developed strategy can be extended to detect other radical-scavenging antioxidants, such as glutathione and vitamin C, offering a versatile and efficient approach for comprehensive analysis of oxidative stress biomarkers and potentially advancing the development of related diagnostic tools.

Conflicts of interest

There are no conflicts to declare.

Data availability

The authors confirm that the data supporting the findings of this study are available within the article.

Supplementary information: Table S1 detection performance of SOD by different analytical methods. Fig. S1 (A) ECL-time curve obtained on NGQDs@NH_2-VMSF/ITO electrode in luminol–DO system in absence or presence of SOD (5 ug/mL). The electrolyte in (A) was 100 μM luminol in 0.01 M PBS, pH = 7.4. (B) ECL-time curve obtained on NGQDs@NH_2-VMSF/ITO electrode in luminol-H_2O_2 system (N_2-purged) without or with SOD (5 ug/mL). The electrolyte contained 100 μM luminol and 100 μM H_2O_2 in N_2-purged PBS (0.01 M, pH = 7.4). Fig. S2 Changes in ECL intensity of NGQDs@NH_2-VMSF/ITO electrode in luminol-H_2O_2 system (N_2-purged) after the addition of BQ (100 μM). The electrolyte contained 100 μM luminol and 100 μM H_2O_2 in N_2-purged PBS (0.01 M, pH = 7.4). Fig. S3 mechanism of ECL process and SOD-based quenching. See DOI: **https://doi.org/10.1039/d5ra07346d**.

Acknowledgements

The authors gratefully acknowledge the National Natural Science Foundation of China (22374130).

References

1 H. Zhao, R. Zhang, X. Yan and K. Fan, *J. Mater. Chem. B*, 2021, **9**, 6939–6957.
2 S. Tamagawa, D. Sakai, H. Nojiri, Y. Nakamura, T. Warita, E. Matsushita, J. Schol, H. Soma, S. Ogasawara, D. Munesada, M. Koike, T. Shimizu, M. Sato, M. Ishijima and M. Watanabe, *Redox Biol.*, 2024, **71**, 103091.
3 Y. Wang, R. Branicky, A. Noë and S. Hekimi, *J. Cell Biol.*, 2018, **217**, 1915–1928.
4 E. Tokuda, Y.-i. Takei, S. Ohara, N. Fujiwara, I. Hozumi and Y. Furukawa, *Mol. Neurodegener.*, 2019, **14**, 42.
5 D. Lazarova, P. Getsov, R. Bakalova, B. Nikolova, S. Semkova, Z. Zhelev, Z. Qiao, T. Ishikawa, K. Fukuda, K. Osada, M. Mileva, T. Mizushima and I. Aoki, *Molecules*, 2025, **30**, 1882.
6 S. D. Gan and K. R. Patel, *J. Invest. Dermatol.*, 2013, **133**, 1–3.
7 M. M.-B. Y. Nuevo Ordoñez, E. Blanco-González and A. Sanz-Medel, *Anal. Chem.*, 2010, **82**, 2387–2394.
8 A. Abdussalam, Y. Chen, F. Yuan, X. Ma, B. Lou and G. Xu, *Anal. Chem.*, 2022, **94**, 11023–11029.
9 X. Fan, J. Wu, T. Zhang and J. Liu, *ChemBioChem*, 2024, **25**, e202400320.
10 H. Chen, J. Huang, R. Zhang and F. Yan, *Front. Chem.*, 2022, **10**, 1023998.
11 Z. Shi, T. Zhang, Y. Zhao, Y. Zhou and J. Liu, *Biosens. Bioelectron.*, 2025, **288**, 117828.
12 T. Zhang, J. Gong, Q. Han, W. Hu, F. Yan and J. Liu, *Talanta*, 2024, **277**, 126319.
13 R. Yu, Y. Zhao and J. Liu, *Nanomaterials*, 2024, **14**, 390.
14 X. Ma, Z. Zhang, Y. Zheng and J. Liu, *Biosensors*, 2024, **14**, 403.
15 J. Huang, S. Xu, F. Yan and J. Liu, *Sens. Actuators, B*, 2024, **402**, 135119.
16 D. Zhong, H. Li, Y. Yang, X. Huang, Z. Yang and C. Wang, *Sens. Actuators, B*, 2026, **446**, 138714.

17 Y. Liu, K. Jiang, Y. Nie, Y. Guo and Q. Ma, *Anal. Bioanal. Chem.*, 2020, **412**, 1893–1899.
18 S. Nam and W.-Y. Lee, *J. Electroanal. Chem.*, 2018, **808**, 59–64.
19 M. Xi, Z. Wu, Z. Luo, L. Ling, W. Xu, R. Xiao, H. Wang, Q. Fang, L. Hu, W. Gu and C. Zhu, *Angew. Chem., Int. Ed.*, 2023, **62**, e202302166.
20 C. Zhao, C. Ma, F. Zhang, W. Li, C. Hong and Y. Qi, *Chem. Eng. J.*, 2023, **466**, 143156.
21 W. Gu, H. Wang, L. Jiao, Y. Wu, Y. Chen, L. Hu, J. Gong, D. Du and C. Zhu, *Angew. Chem., Int. Ed.*, 2020, **59**, 3534–3538.
22 J. An, C. Zhang, F. Yan and P. Ma, *Microchem. J.*, 2024, **206**, 111413.
23 F. A. Bushira, P. Wang and Y. Jin, *Anal. Chem.*, 2022, **94**, 2958–2965.
24 H. Xia, X. Zheng, J. Li, L. Wang, Y. Xue, C. Peng, Y. Han, Y. Wang, S. Guo, J. Wang and E. Wang, *J. Am. Chem. Soc.*, 2022, **144**, 7741–7749.
25 F. A. Bushira, P. Wang, Y. Wang, S. Hou, X. Diao, H. Li, L. Zheng and Y. Jin, *Anal. Chem.*, 2022, **94**, 9758–9765.
26 X. Fan, T. Zhang, S. Wang, Y. Jiang, Y. Zhao, F. Yan and F. Xi, *Sens. Actuators, B*, 2025, **439**, 137856.
27 C. Zhu, Y. Zhao and J. Liu, *Biosensors*, 2025, **15**, 63.
28 R. Eivazzadeh-Keihan, E. Bahojb Noruzi, E. Chidar, M. Jafari, F. Davoodi, A. Kashtiaray, M. Ghafori Gorab, S. Masoud Hashemi, S. Javanshir, R. Ahangari Cohan, A. Maleki and M. Mahdavi, *Chem. Eng. J.*, 2022, **442**, 136183.
29 Y. Cui, S. Zhang, X. Zhou, F. Yan and W. Hu, *Microchem. J.*, 2023, **190**, 108632.
30 W. Zheng, R. Su, G. Yu, L. Liu and F. Yan, *Nanomaterials*, 2022, **12**, 3632.
31 H. Zhou, X. Ma, A. Sailjoi, Y. Zou, X. Lin, F. Yan, B. Su and J. Liu, *Sens. Actuators, B*, 2022, **353**, 131101.
32 Q. Han, T. Zhang, M. Wang, F. Yan and J. Liu, *Molecules*, 2022, **27**, 8200.
33 C. Zhu, H. Wang and J. Liu, *Front. Chem.*, 2025, **13**, 1549927.
34 Y. Zou, X. Zhou, L. Xie, H. Tang and F. Yan, *Front. Chem.*, 2022, **10**, 939510.
35 J. Xing, H. Wang and F. Yan, *Molecules*, 2024, **29**, 4334.
36 X. Deng, X. Lin, H. Zhou, J. Liu and H. Tang, *Nanomaterials*, 2023, **13**, 239.
37 J. Gong, H. Tang, M. Wang, X. Lin, K. Wang and J. Liu, *Mater. Des.*, 2022, **215**, 110506.
38 H. Zhou, G. Dong, A. Sailjoi and J. Liu, *Nanomaterials*, 2022, **12**, 65.
39 C. Huang, S. Zhang, X. Ma, F. Yan and W. Tang, *Nanomaterials*, 2024, **14**, 569.
40 J. Zhang, L. Yang, J. Pei, Y. Tian and J. Liu, *Front. Chem.*, 2022, **10**, 939736.
41 H. Lu, W. Li, H. Dong and M. Wei, *Small*, 2019, **15**, 1902136.
42 Y. Zheng, J. Lin, L. Xie, H. Tang, K. Wang and J. Liu, *Front. Chem.*, 2021, **9**, 688358.
43 L. Wang, Q. Sun, J. Wang, J. Zhou, J. Liu, Z. Zhang and F. Yan, *Anal. Methods*, 2025, **17**, 7628–7634.
44 S. Xu, S. Zhang, Y. Li and J. Liu, *Molecules*, 2023, **28**, 6064.
45 J. Wu, T. Zhang, X. Jia, J. Li, H. Xie, F. Yan, D. Li and J. Liu, *J. Colloid Interface Sci.*, 2026, **701**, 138721.
46 J. Huang, X. Fan, F. Yan and J. Liu, *ACS Appl. Nano Mater.*, 2024, **7**, 7743–7752.
47 P. Zhou, L. Yao, K. Chen and B. Su, *Crit. Rev. Anal. Chem.*, 2019, **50**, 424–444.
48 X. Luo, T. Zhang, H. Tang and J. Liu, *Front. Nutr.*, 2022, **9**, 962736.
49 J. Huang, T. Zhang, G. Dong, S. Zhu, F. Yan and J. Liu, *Front. Chem.*, 2022, **10**, 900282.
50 D. Li, S. Xu, H. Jin, J. Wang and F. Yan, *Molecules*, 2023, **28**, 7515.
51 Q. Guo, X. Fan, F. Yan and Y. Wang, *Front. Chem.*, 2023, **11**, 1271556.
52 N. Ma, S. Xu, W. Wu and J. Liu, *Molecules*, 2023, **28**, 7664.
53 J. Huang, T. Zhang, Y. Zheng and J. Liu, *Biosensors*, 2023, **13**, 317.
54 A. Walcarius, *Acc. Chem. Res.*, 2021, **54**, 3563–3575.
55 C. Wei, Y. Zheng, F. Yan and L. Xu, *Biosensors*, 2025, **15**, 332.
56 C. Zhang, X. Zhou, F. Yan and J. Lin, *Molecules*, 2023, **28**, 6443.
57 L. Yang, T. Zhang, H. Zhou, F. Yan and Y. Liu, *Front. Nutr.*, 2022, **9**, 987442.
58 W. Zheng, R. Su, X. Lin and J. Liu, *Front. Chem.*, 2022, **10**, 954802.
59 Y. Zhang, S. Zhang, J. Liu and D. Qin, *Molecules*, 2023, **28**, 6935.
60 X. Zhou, X. Gu, S. Zhang, Y. Zou and F. Yan, *Microchem. J.*, 2024, **200**, 110315.
61 K. Ma, L. Yang, J. Liu and J. Liu, *Nanomaterials*, 2022, **12**, 1157.
62 J. Gong, T. Zhang, P. Chen, F. Yan and J. Liu, *Sens. Actuators, B*, 2022, **368**, 132086.
63 M. T. Hasan, R. Gonzalez-Rodriguez, C. Ryan, N. Faerber, J. L. Coffer and A. V. Naumov, *Adv. Funct. Mater.*, 2018, **28**, 1804337.
64 J. Zhao, X. Gu and J. Liu, *Microchem. J.*, 2025, **216**, 114671.
65 Z. Yan, L. Wang and F. Yan, *Molecules*, 2025, **30**, 1347.
66 J. Gong, T. Zhang, T. Luo, X. Luo, F. Yan, W. Tang and J. Liu, *Biosens. Bioelectron.*, 2022, **215**, 114563.
67 X. Fan, L. Wang, H. Wang, L. Huang, J. Lin, X. Gao and F. Xi, *Biosens. Bioelectron.*, 2025, **280**, 117451.
68 N. Gao, G. Ren, M. Zhang and L. Mao, *J. Am. Chem. Soc.*, 2024, **146**, 3836–3843.
69 X. Zhou, Y. Zou, H. Ru, F. Yan and J. Liu, *Anal. Chem.*, 2024, **96**, 10264–10273.
70 Y. Zhou, C. Zhang, J. Liu and Y. Mou, *Talanta*, 2025, **285**, 127223.
71 Z. Lin, L. Huang, Y. Liu, J.-M. Lin, Y. Chi and G. Chen, *Electrochem. Commun.*, 2008, **10**, 1708–1711.
72 Y. Lin, H. Dai, G. Xu, T. Yang, C. Yang, Y. Tong, Y. Yang and G. Chen, *Microchim. Acta*, 2013, **180**, 563–572.
73 J. Wang, Z. Jiang, L. Xie, M. Liu and Y. Yuan, *Microchim. Acta*, 2016, **184**, 289–296.
74 M. Saqib, L. Qi, P. Hui, A. Nsabimana, M. I. Halawa, W. Zhang and G. Xu, *Biosens. Bioelectron.*, 2018, **99**, 519–524.